



Rapid and complete inactivation of pathogenic microorganisms by solar-assisted in-situ H_2O_2 generation using a polypyrrole-supported copper sulfide system

Zhuoyun Tang^a, Wei Qu^a, Zhuohang Lin^a, Junjie Li^a, Peizhi Wu^a, Qiyu Lian^a, Chun He^{a,b}, Ran Yin^{c,*}, Po Keung Wong^d, Dehua Xia^{a,b,**}

^a School of Environmental Science and Engineering, Sun Yat-sen University, Guangzhou 510275, China

^b Guangdong Provincial Key Laboratory of Environmental Pollution Control and Remediation Technology, Guangzhou 510275, China

^c Department of Civil and Environmental Engineering, The Hong Kong University of Science and Technology, Clear Water Bay, Kowloon, Hong Kong, China

^d School of Life Sciences, The Chinese University of Hong Kong, Shatin, NT, Hong Kong, China

ARTICLE INFO

Keywords:

Fenton-like reactions
Bond bridge
Dual reaction centers
Electron extraction
Viable but nonculturable

ABSTRACT

In this study, we report a photo-assisted H_2O_2 self-supply and in-situ activation system based on the polypyrrole-supported copper sulfide (solar/ $Cu_{2-x}S@PPy$) for water disinfection. 6.57-log, 4.22-log, and 5.23-log inactivation of *Escherichia coli* K-12 (even at a viable but nonculturable state), *Bacillus subtilis* spores, and bacteriophage MS2 are achieved within 60 min by using the solar/ $Cu_{2-x}S@PPy$ system in batch and flow-through reactors. Catalyst characterization and theoretical calculation results suggest that the photo-generated H_2O_2 is in-situ activated by the Cu–N bridges in $Cu_{2-x}S@PPy-H_2O_2$ is oxidized to $\bullet O_2$ and ultimately 1O_2 on Cu sites, and electrons are subsequently pumped to electron-rich N sites ($H_2O_2 \rightarrow Cu \rightarrow N$) to maintain the balance of electron donation-acquisition. The electrons can be directly extracted from cell membranes to $Cu_{2-x}S@PPy$, making cells vulnerable to reactive oxygen species and heat. This work provides a novel and affordable solution for the rapid disinfection of drinking water in rural and underdeveloped areas.

1. Introduction

Pathogenic microorganisms (e.g., bacteria, spores, and viruses) contaminate drinking water sources and pose direct health threats to water consumers [1,2]. Effective, affordable, and sustainable disinfection technologies are urgently needed to achieve Sustainable Development Goal No. 6.1 (SDG 6.1). Conventional disinfection technologies including chlorination, ozonation, and UV irradiation have intrinsic limitations. For example, they would produce toxic byproducts (halogenated byproducts and bromate), lead to incomplete inactivation (pathogens stay at viable but nonculturable (VBNC) state and would remain self-repair ability and virulence), or require expensive equipment and apparatus (e.g., UV setups) [3–5]. Conventional solar disinfection (SODIS) is a low-cost, chemical-free, and user-friendly approach, but it usually takes a long time to achieve the desired disinfection targets (e.g., 6-log inactivation) and can be easily affected by the water quality and operational conditions (e.g., weather conditions) [6,7].

Fenton-like processes are increasingly investigated and practiced for water disinfection owing to their high efficiency, relatively low cost, and simple operation [6,8]. However, conventional Fenton-like processes depending on single-metal centers are limited by the low cycle conversion rate of $M^{(n+m)+}/M^{n+}$, high dissolution of metal ions, and inefficient operation in the long-term run [9]. Additionally, Fenton-like processes require a large consumption of H_2O_2 and narrow operating pH, which limits their large-scale applications. In those contexts, constructing highly efficient, low-cost, and low carbon-footprint Fenton-like systems that can realize the self-supply and in-situ activation of H_2O_2 is of great significance.

Dual (electron-rich/poor) reaction centers can activate H_2O_2 and maintain the dynamic balance of electrons via electron transfer among dual centers, oxidants, and pollutants, which breaks constraints of narrow pH range and slow metal cycling rate of conventional Fenton-like systems [10]. Our previous work constructed the oxygen-vacancy-rich BiOX (X = Cl and I) as dual-reaction-center Fenton-like catalysts,

* Corresponding author.

** Corresponding author at: School of Environmental Science and Engineering, Sun Yat-sen University, Guangzhou 510275, China.

E-mail addresses: ryin@connect.ust.hk (R. Yin), xiadehua3@mail.sysu.edu.cn (D. Xia).

which remained high reactivity in long-term running under neutral conditions [11,12]. Notably, although $\bullet\text{OH}$ activated by H_2O_2 has a relatively high redox potential ($E_0 = 2.80 \text{ V/NHE}$), it has a short lifetime ($< 200 \text{ ns}$) and will be easily quenched by organic matters in water, which greatly affects the disinfection performance [13,14]. Thus, dominating reactions by nonradical pathways (e.g., $^1\text{O}_2$ and electron transfer) through the construction of dual reaction centers has attracted growing attention, since those processes have lower oxidant demand and are less sensitive to water matrix components [15,16]. Li et al. have established a nonradical Fenton-like system over $\text{g-C}_3\text{N}_4/\text{MgO}$ for sulfamethoxazole degradation, in which N-Mg bonds with strong electron absorbance ability activated H_2O_2 to $^1\text{O}_2$ [17]. Motivated by these works, developing a dual-reaction-center Fenton-like process with nonradical pathways is worth further research in the field of disinfection.

Meanwhile, the excessive consumption of H_2O_2 and risks during transportation and storage are other issues in conventional Fenton-like systems. Previous studies reported that carbon nitride compounds have promising photocatalytic H_2O_2 production ability [18–20]. Among them, polypyrrole (PPy) is a conjugated polymer, which has low cost and high thermal stability and is easy to be synthesized with negligible toxicity [21,22]. Moreover, PPy with positive charges and high conductivity is an excellent electrical conducting polymer and has electrostatic interaction with bacterial cells, which is expected to directly extract electrons from cell membranes, damage the membranes, and enhance disinfection efficiency. Upon generation, the activation of the generated H_2O_2 can generate reactive oxygen species (ROSs) and enhance the disinfection performance. Metal sulfides (e.g., Cu_{2-x}S) are promising catalysts for H_2O_2 activation. The reasons are listed below: (i) metal sulfides are abundant in natural minerals and cheap, among which Cu_{2-x}S is one of the main copper mineral resources; (ii) As a semiconductor material, Cu_{2-x}S has good optoelectronic behavior, nontoxic nature, and a degree of biodegradability, which has been used for photocatalytic, biomedical, and biosensing applications [23,24]; and (iii) Cu_{2-x}S has many intertwined sheet-like units on the surface which can accelerate interfacial electron transfer [25]. Due to those promising properties, we can combine PPy with Cu_{2-x}S to realize continuous H_2O_2 generation/activation. Additionally, previous studies have proposed an “electron pump” strategy to realize interfacial directional electron transfer via a strong interaction binding [26–28]. For example, Liu et al. combined amorphous iron oxide support with single-atom Ru, and Ru served as an “electron pump” via the d(Ru)-d(Fe) coupling to enrich photo-generated electrons for nitrogen photofixation [27]. Similarly, we hypothesize that PPy can serve as an “electron pump” to attract electrons transfer from Cu_{2-x}S via a bond bridge to realize H_2O_2 activation via the electron redistribution for long-term enhanced disinfection.

To verify the hypotheses and fill the knowledge gaps as above-mentioned, we grew PPy chains on Cu_{2-x}S ($\text{Cu}_{2-x}\text{S}@PPy$) to realize a “one-stone-three-birds” manner: (i) It realized in-situ H_2O_2 generation; (ii) PPy served as an “electron pump” to gain excess electrons from Cu sites during H_2O_2 activation via the interfacial bond bridges to ensure the stability of Cu active sites; and (iii) when cells served as an “electron reservoir”, $\text{Cu}_{2-x}\text{S}@PPy$ could extract electrons from cell membranes. The inactivation efficiencies of three representative pathogenic microorganisms (*Escherichia coli* K-12, *Bacillus subtilis* spores, and bacteriophage MS2) by the solar/ $\text{Cu}_{2-x}\text{S}@PPy$ system were assessed in synthetic and real surface water under real sunlight. The mechanisms of in-situ H_2O_2 generation and activation were revealed by comprehensive characterizations of the catalyst and density functional theory (DFT) calculations. Moreover, the bacterial inactivation process was explored thoroughly by detecting the extracellular electron transfer (EET) manner and biological changes at molecular levels. Some previous studies reported using cheaper materials (e.g., biochar) for water sterilization (Table S1) [29,30]. Compared to the existing sterilization systems, the solar/ $\text{Cu}_{2-x}\text{S}@PPy$ system can rapidly and completely inactivate pathogens. Its self-supply ability of H_2O_2 requires no

additional inputs of oxidants. The use of solar light as the driving force further increases the sustainability and adaptivity of the process for water sterilization in underdeveloped areas.

2. Experimental section

2.1. Chemicals and preparation of catalysts

The chemicals and reagents used in this work are presented in Text S1 in Supporting Information (SI). The synthetic process of $\text{Cu}_{2-x}\text{S}@PPy$ is provided in Text S2 in SI. The methods used for the characterizations of catalysts are presented in Text S3 in SI.

2.2. Disinfection experiments in batch and flow-through reactors

In the batch tests, catalysts (0.2 mg/mL) and as-prepared microbial suspensions (Text S5) were mixed first in a 25 mL reactor containing synthetic surface water (2 mM phosphate-buffered saline). The light source was a Xenon lamp (PLS-SXE300D, Beijing Perfectlight Technology Co., Ltd.). At predetermined time intervals, samples were collected and subjected to analysis of residual microbial concentrations. The disinfection performance was also evaluated in a plastic bottle reactor and a flow-through reactor under natural sunlight. In the flow-through reactor, raw water was mixed with $\text{Cu}_{2-x}\text{S}@PPy$, then flowed into the flow-through reactor under gravity (flow rate $\approx 1.4 \text{ L/h}$), followed by sterilization under sunlight from 10:00–17:00. The concentration of culturable bacteria can be confirmed via a standard plate counting method. Detailed disinfection experiments are in Texts S6–S7. In addition to synthetic surface water, experiments were also conducted in a similar manner by using real surface water. The surface water sample was collected from the Pearl River in Guangzhou, China (23.07°N, 113.39°E), and the properties of the surface water are displayed in Table S2. The details of experimental procedures and the determination of water quality parameters are shown in Text S8 in SI. It is noted that the Xenon lamp was only served as the light source in the batch reactor to control the light intensity. All the disinfection tests in the plastic bottle and flow-through reactor were performed under natural solar light and the light intensity was recorded in Fig. S13.

To examine changes in the VBNC state of the microorganisms before and after disinfection, D_2O -labeled confocal Raman microspectroscopy (inVia Qontor, Renishaw, UK) measurement was conducted to determine the change of cellular activity. More details of the operational procedures are shown in Text S10 in SI.

2.3. Experiments for identification of extracellular electron transfer pathway

- (1) Electrochemical tests: The linear sweep voltammetry (LSV) curves were measured by the CHI-660E electrochemical workstation with a system containing three-electrode quartz cells. The sample coated on stainless steel wire was served as the working electrode. 100- μL of bacterial suspensions ($\sim 7 \log_{10} \text{ cfu/mL}$) was dropped on samples, followed by drying at 37°C for 0.5 h to form bacterial membranes. The dead bacterial suspensions were pre-treated with 4% paraformaldehyde for 2 h.
- (2) Kelvin probe force microscopy (KPFM) measurement: $\text{Cu}_{2-x}\text{S}@PPy$ was pressed into flakes by a tablet press. Subsequently, 10 μL of bacterial suspensions were evenly dropped on the sample slices and dried in air for 5 min before KPFM measurements [31].
- (3) Detection of cell membrane potential: The cell membrane potential was explored by using 3, 3'-diethyloxa-carbocyanine iodides ($\text{DiOC}_2(3)$) as a fluorescence probe, and details are in Text S14.

Moreover, H_2O_2 production measurement (Text S4), the acute and

genetic toxicity evaluation (Text S11), theoretical simulation/calculation (Texts S12–S13), and cellular biological analysis (Text S15) are presented in SI.

3. Results and discussion

3.1. Characterizations

3.1.1. Physicochemical properties

$\text{Cu}_{2-x}\text{S}@PPy$ was obtained through a simple solvothermal approach and polymerization procedure (Fig. 1a) [25]. The crystalline phase structures were detected by the X-ray diffraction (XRD) technique. PPy has an amorphous structure with a broad and weak reflection in the range of $15\text{--}30^\circ$ (Fig. S1), while Cu_{2-x}S can be well-fitted to the covellite

structure (Fig. 1b) [32]. $\text{Cu}_{2-x}\text{S}@PPy$ has a similar pattern with Cu_{2-x}S and shows an additional broad reflection peak at $15\text{--}30^\circ$. It proved that PPy was successfully deposited on Cu_{2-x}S . As shown in scanning electron microscopy (SEM) images (Fig. 1c and S2), Cu_{2-x}S particles are 3D hollow microspheres with an average diameter of $2\text{ }\mu\text{m}$. Many intertwined sheet-like units are on the surface of Cu_{2-x}S . After chemical polymerization, PPy partly covers Cu_{2-x}S and even inserts into its sheet-like unit structure (Fig. 1d). It will facilitate the electron transfer from Cu_{2-x}S layer edges to PPy [25]. Additionally, the resulting rough surface is beneficial for capturing bacterial cells due to topological interactions [33,34]. Mapping images in Fig. 1e further confirm the distribution of Cu, S, C, and N.

Fourier transform infrared (FTIR) spectra, X-ray photoelectron (XPS) spectroscopy, and solid-state electron paramagnetic resonance (EPR)

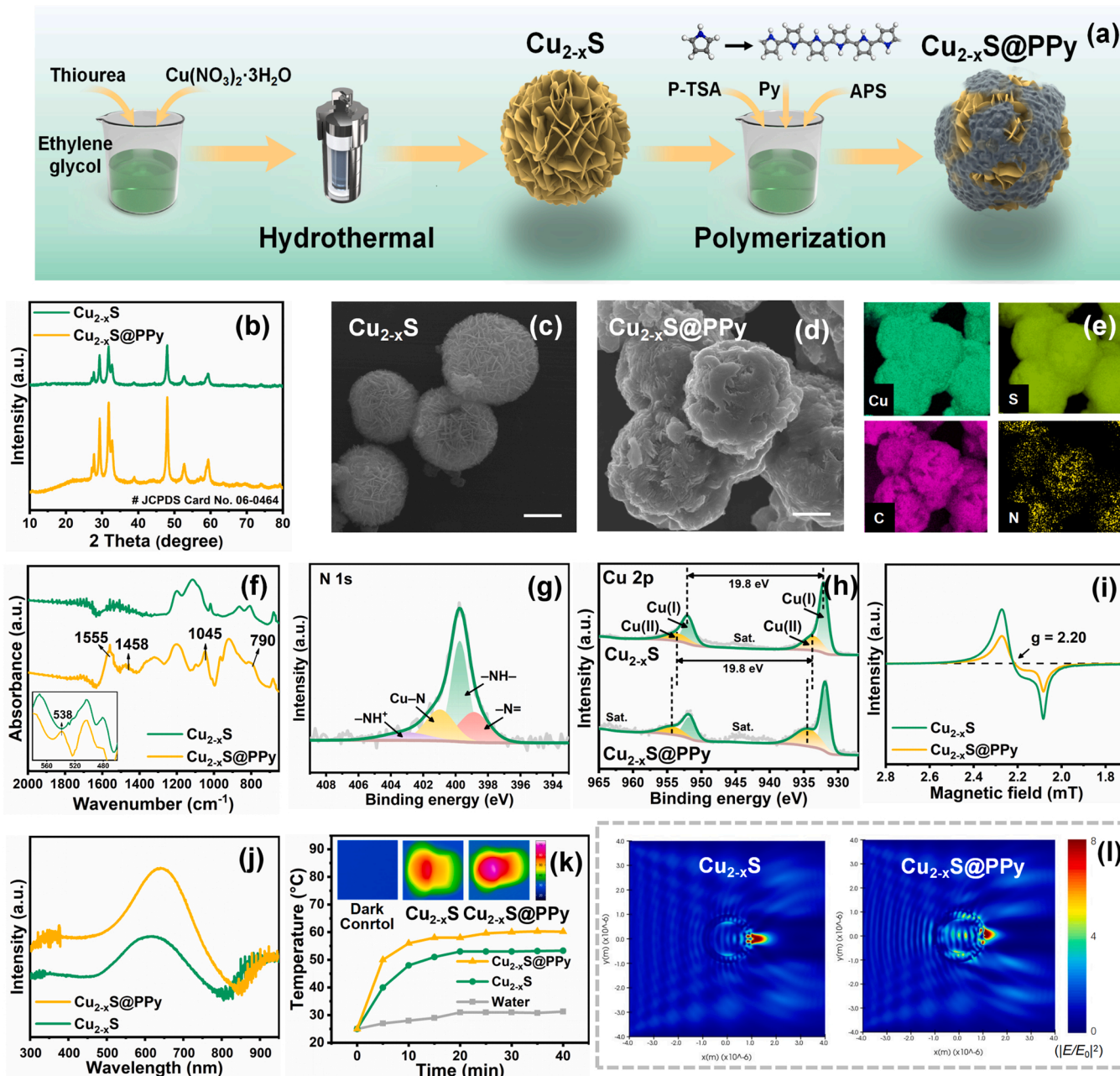


Fig. 1. (a) Schematic illustration of the synthesis process of $\text{Cu}_{2-x}\text{S}@PPy$; XRD patterns (b), SEM images (c–d), and mapping images (e) of Cu_{2-x}S and $\text{Cu}_{2-x}\text{S}@PPy$ (scale bar = $1\text{ }\mu\text{m}$); FTIR spectra (f), high-resolution XPS spectra of N 1s (g) and Cu 2p (h), solid-state EPR spectroscopy (i), and UV–vis–NIR absorption spectra (j) of Cu_{2-x}S and $\text{Cu}_{2-x}\text{S}@PPy$; (k) Temperature versus time plots recorded in water and solid-state infrared thermographic images (inset); (l) Electromagnetic field distribution at the cross-sections of Cu_{2-x}S and $\text{Cu}_{2-x}\text{S}@PPy$ in water via the FDTD simulation.

spectra were involved to further explore interactions between Cu_{2-x}S and PPy. From Fig. 1 f, the FTIR pattern of $\text{Cu}_{2-x}\text{S}@PPy$ shows the vibration of Cu–N bonds at 538 cm^{-1} , which indicated the chemical interaction between Cu_{2-x}S and PPy [35]. Additionally, characteristic peaks at 1555 and 1458 cm^{-1} are attributed to the antisymmetric and symmetric PPy ring-stretching modes, respectively, while peaks at 1045 and 790 cm^{-1} are related to the in-plane and out-of-plane vibrations of C–H deformation [36,37]. The high-resolution N 1s XPS spectrum of $\text{Cu}_{2-x}\text{S}@PPy$ (Fig. 1 g) can be divided into four peaks. The peak at 400.9 eV is ascribed to the Cu–N coordination, while the other three peaks at 402.9 , 399.9 , and 398.6 eV are for positively charged nitrogen ($-\text{NH}^+$), pyrrole nitrogen ($-\text{NH}-$) and imine-like structure ($-\text{N}=\text{}$), respectively [35,36,38]. It implies that part of pyrrole N in PPy chains forms covalent bonds with Cu atoms. In the Cu 2p spectrum of Cu_{2-x}S (Fig. 1 h), two peaks at 932.1 (Cu $2p_{3/2}$) and 951.9 eV (Cu $2p_{1/2}$) are attributed to Cu^+ , and peaks at 933.7 (Cu $2p_{3/2}$) and 953.5 eV (Cu $2p_{1/2}$) correspond to Cu^{2+} [38–40]. The satellite peak at $\sim 944.3\text{ eV}$ is associated with Cu^{2+} [41]. Similarly, in Cu LM2 Auger spectra (Fig. S6), the kinetic energies at 916.2 eV and 918.4 eV correspond to Cu^+ and Cu^{2+} , respectively [42]. Notably, the binding energy of Cu^{2+} of $\text{Cu}_{2-x}\text{S}@PPy$ exhibits higher energy than that of Cu_{2-x}S (Fig. 1 h) because N has a higher electronegativity than that of Cu and outermost electrons of Cu tend to transfer to electron-rich N sites [43,44]. The electron distribution of catalysts was detected by EPR spectroscopy. In Fig. 1i, the g value of the broad peak in Cu_{2-x}S is located at ~ 2.20 , which is attributed to the covalent character of Cu(II)-ligand, and unpaired electrons localized in the dx^2-y^2 orbital of Cu(II) [45–47]. The peak intensity of $\text{Cu}_{2-x}\text{S}@PPy$ is lower than that of Cu_{2-x}S , implying that the single electron density decreases around Cu sites owing to the Cu–N coordination structure [47]. The results implied the formation of electron-poor Cu and electron-rich N centers. The newly formed Cu–N bridges were anticipated to participate in electron migration during H_2O_2 activation and contribute to bacterial inactivation, which will be discussed in the “mechanisms” sections.

3.1.2. Photoabsorption and photothermal properties

As shown in UV–vis–NIR absorption spectra (Fig. 1j), Cu_{2-x}S has strong light absorption in visible and NIR regions. The light absorption intensity of $\text{Cu}_{2-x}\text{S}@PPy$ is further enhanced because PPy has black monolithic and conjugated structures with $\pi-\pi^*$ transition [36]. Moreover, the distribution and intensity of electromagnetic fields under incident light were simulated via the finite difference time domain (FDTD) simulation. As shown in Fig. 1 l and S7, the intensity of electromagnetic fields increases on the surface and in the cavity of the Cu_{2-x}S hollow microsphere. It implies that the multiple scattering effect improves its light-harvesting efficiency [48]. Moreover, $\text{Cu}_{2-x}\text{S}@PPy$ has higher intensity and spatial uneven level of electromagnetic fields under irradiation, suggesting that it has a higher formation and separation rate of electron-hole pair [49]. The enhanced built-in electric field between Cu_{2-x}S and PPy will promote the electron transfer process [50]. Moreover, according to the Kubelka-Munk plots (Fig. S8), the calculated bandgap of Cu_{2-x}S and $\text{Cu}_{2-x}\text{S}@PPy$ is 1.32 and 1.29 eV , respectively [51,52]. Thus, PPy narrows the bandgap and is beneficial for sunlight absorption and charge separation. Based on the Mott-Schottky plots (Fig. S9), their conduction bands (CB) were -0.48 and -0.35 eV . The valence bands (VB) were estimated to be $+0.84$ and $+0.94\text{ eV}$, respectively.

As for detecting the photothermal conversion ability, localized heat on catalysts' surfaces was investigated by an infrared thermo-camera. Cu_{2-x}S has good light-to-heat ability due to the d-d band transition of Cu and the surface plasmon resonance (SPR) effect from the inherent Cu vacancies [23]. Thus, the interfacial temperature can reach 60°C after 10-min irradiation (the inset of Fig. 1k). Notably, the interfacial temperature of $\text{Cu}_{2-x}\text{S}@PPy$ rose significantly to over 70°C , confirming that PPy increased thermal energy. The temperature evolution in water was also monitored. From Fig. 1k, the temperature of pure water is only

increased by around 6°C from the room temperature (ca. 25°C) after 40-min irradiation. After adding Cu_{2-x}S and $\text{Cu}_{2-x}\text{S}@PPy$, the temperature increased promptly to 53.3 and 60.2°C , respectively. Notably, the local temperature above 51°C may cause thermal protein deformation and even thermo-mechanical damage to *Escherichia coli* (*E. coli*) [53].

3.2. Disinfection performance of the solar/ $\text{Cu}_{2-x}\text{S}@PPy$ system

3.2.1. Inactivation of representative microorganisms in batch reactors

The disinfection efficiency of the solar/ $\text{Cu}_{2-x}\text{S}@PPy$ system was tested in a batch reactor in synthetic surface water first. Dark control tests suggested that Cu_{2-x}S , PPy, and $\text{Cu}_{2-x}\text{S}@PPy$ have almost no effect on microbial activity (Fig. S10). As shown in Fig. 2a, an insignificant amount (0.19 cfu/mL) of *E. coli* cells were inactivated after 40 min by solar irradiation without catalysts, confirming that the conventional SODIS by solar irradiation alone was ineffective in disinfection. Notably, the solar/ $\text{Cu}_{2-x}\text{S}@PPy$ system can inactivate $6.57\log_{10}\text{ cfu/mL}$ of culturable cells within 40-min irradiation, much higher than that of the solar/ Cu_{2-x}S ($3.02\log_{10}\text{ cfu/mL}$) and solar/PPy ($1.20\log_{10}\text{ cfu/mL}$) systems. Owing to the good photothermal conversion ability of $\text{Cu}_{2-x}\text{S}@PPy$, the temperature in water bulk was heated to 60.2°C after 40-min solar/ $\text{Cu}_{2-x}\text{S}@PPy$ treatment (Fig. 1k). Thus, to explore the contribution of heat to disinfection, the $\text{Cu}_{2-x}\text{S}@PPy$ mixture was kept in a water bath at 25°C (i.e., the room temperature) to eliminate the photothermal effect under light irradiation, and it only reduced $3.32\log_{10}\text{ cfu/mL}$ of culturable bacteria (Fig. S11). It indicated that the synergy between photothermal and photocatalytic processes existed in the system. By gradually increasing the water bath temperature (from 10°C to 60°C) in the photocatalytic processes, we found that the higher temperature greatly accelerated the disinfection process (Fig. S11). Furthermore, the solar/ $\text{Cu}_{2-x}\text{S}@PPy$ system exhibited considerable broad-spectrum disinfection ability, which can inactivate $4.22\log_{10}\text{ cfu/mL}$ of *Bacillus subtilis* spores and $5.23\log_{10}\text{ pfu/mL}$ of bacteriophage MS2 within 60 min (Fig. S12).

Considering that some treated bacterial cells may enter into a VBNC state and pose a potential threat to human beings, the viability of VBNC cells was further explored via the D_2O -labeled confocal Raman analysis [54,55]. VBNC cells can uptake D_2O and nutrients to form components with C–D bonds after a period of incubation, which exhibits a broad peak ($2040\text{--}2300\text{ cm}^{-1}$) in Raman spectra [54]. From Fig. 2b, the Raman spectra of bacterial cells before treatment show a distinguished characteristic peak of C–D bonds because cells had good metabolic activity. The C–D peak disappeared after 40-min solar/ $\text{Cu}_{2-x}\text{S}@PPy$ treatment. It indicated that cells, including VBNC cells, completely lost their self-repair capability and dead. The C–D/(C–D + C–H) ratio in Raman spectra can quantitatively reflect cellular metabolic activity during disinfection [55]. As shown in Fig. 2c, the ratios of untreated samples without/with introducing D_2O were 0.40% and 19.62% , respectively. After 40-min treatment, it dramatically dropped to 0.92% , indicating that the vast majority of cells including VBNC cells lost their metabolic activity and were completely inactivated. The efficiency is higher than the previous studies [56,57]. We assume that the reasons responsible for its boosting performance were the increased ROSs level and specific bactericidal actions of $\text{Cu}_{2-x}\text{S}@PPy$ to bacterial cells, which will be discussed in the “mechanisms” sections.

3.2.2. Disinfection under natural sunlight and in real surface water

Disinfection tests were also carried out in portable plastic and quartz bottles (Fig. 2d) under natural sunlight to further develop real-world applications for emergency purposes in wild or disaster-stricken areas. Changes in optical power density with exposure time were recorded in Fig. S13 and the average optical power density was around 710 W/m^2 . In addition, experiments were conducted using the real surface water (SW) collected locally (the water quality was listed in Table S2) to demonstrate the disinfection efficiency under real environmental and operational conditions.

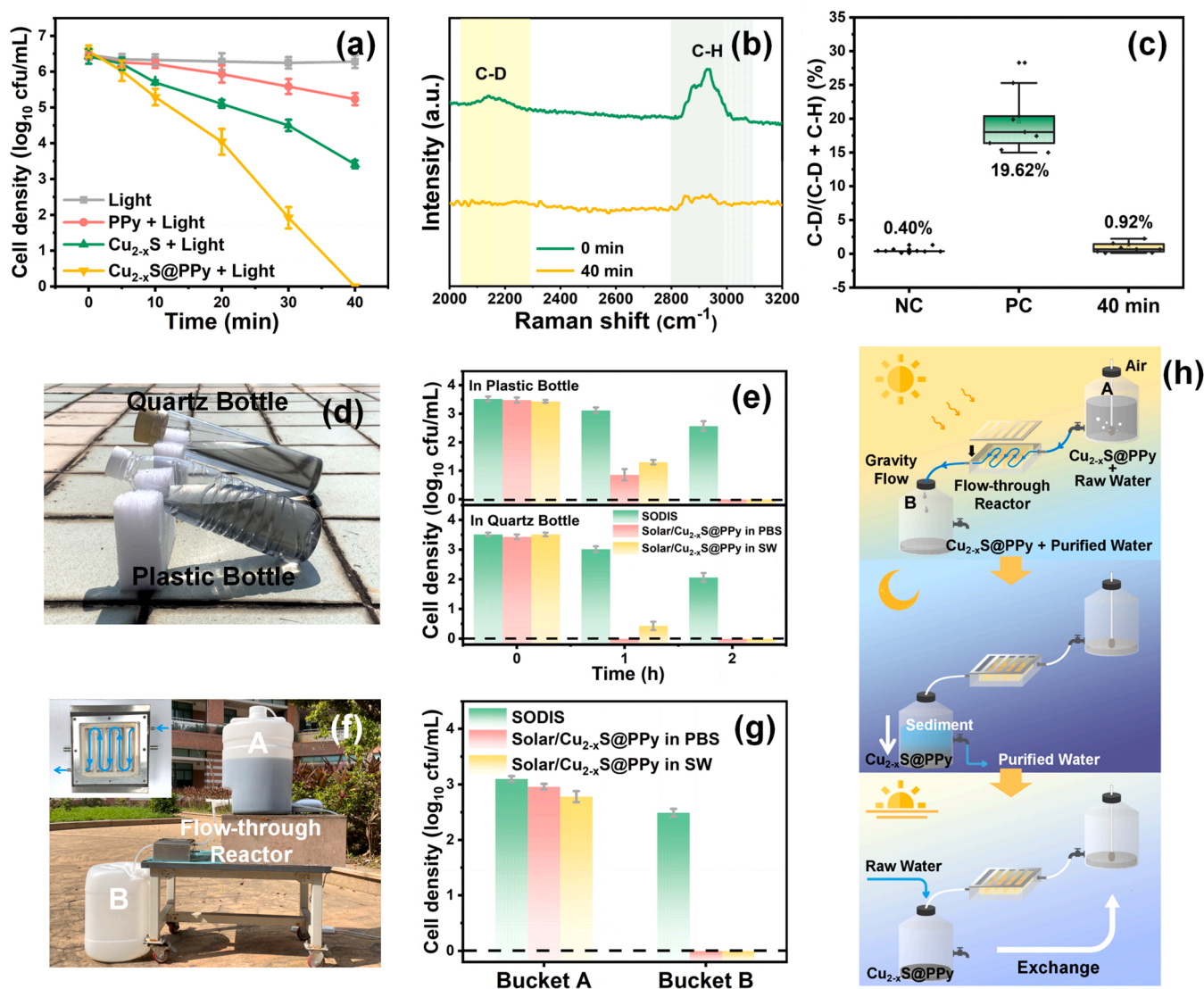


Fig. 2. (a) Inactivation of *E. coli* K-12 with Cu_{2-x}S , PPy, and $\text{Cu}_{2-x}\text{S}@PPy$ under irradiation; D_2O -labeled confocal Raman micro-spectroscopy (b) and the corresponding ratios of C-D/(C-D + C-H) (c) of *E. coli* K-12 before/after the solar/ $\text{Cu}_{2-x}\text{S}@PPy$ treatment (the untreated samples incubated in the absence/presence of D_2O were expressed as the negative control (NC)/positive control (PC), experimental conditions: [PPy] = [Cu_{2-x}S] = [$\text{Cu}_{2-x}\text{S}@PPy$] = 0.2 mg/mL, optical power density $\approx 2000 \text{ W/m}^2$, pH = 7); Actual photograph (d) and bactericidal efficiency (e) of the solar/ $\text{Cu}_{2-x}\text{S}@PPy$ system in a quartz bottle (QB) and plastic bottle (PB) under natural sunlight; Operation photograph (f) and bactericidal capability (g) of the solar/ $\text{Cu}_{2-x}\text{S}@PPy$ system in the flow-through reactor; (h) Workflow of the flow-through disinfection reactor with SSRS.

As shown in Fig. 2e, in plastic bottles, 2.62 and 2.13 \log_{10} cfu/mL of *E. coli* K-12 were inactivated by the solar/ $\text{Cu}_{2-x}\text{S}@PPy$ process after 1 h in synthetic surface water and real surface water, respectively. The inactivation rate was much higher than that of SODIS alone (0.40 \log_{10} cfu/mL). The slightly worse inactivation rate in real surface water than the synthetic water was likely because of the lighter filtering and reactive species scavenging effects of the matrix components (e.g., turbidity and dissolved organic matter) in real surface water. After 2-h treatment, the *E. coli* K-12 cells were completely inactivated by the solar/ $\text{Cu}_{2-x}\text{S}@PPy$ process in synthetic and real surface water, while only 0.95 \log_{10} cfu/mL of *E. coli* K-12 cells were inactivated by SODIS alone. The temperature increased to 50.3 $^{\circ}\text{C}$ after 2-h solar/ $\text{Cu}_{2-x}\text{S}@PPy$ treatment (Fig. S14). The promising disinfection performance was also observed by using quartz bottles (Fig. 2e). The better performance of using quartz bottles than using plastic bottles was likely because the light penetration was better in quartz bottles. Notably, when batch reactors are used, the separation of the catalysts from the purified water can be easily achieved by several hours of settling (Fig. S16).

Furthermore, we also fabricated a flow-through reactor under real solar light and equipped it with a standing separation-recycling system (SSRS) (Fig. 2f) for potential household applications in undeveloped areas. Its workflow is shown in Fig. 2h and Text S7. Briefly, raw water mixed with $\text{Cu}_{2-x}\text{S}@PPy$ would flow into the flow-through reactor under gravity under sunlight and meet standing overnight to realize the separation between catalysts and water. Around wt. 99.9% of catalysts were separated from the purified water after standing overnight (Fig. S16c). On the following morning, raw water was mixed with the residual $\text{Cu}_{2-x}\text{S}@PPy$ again, and the disinfection workflow continued to work. After 1-cycle treatment, 2.96 and 2.68 \log_{10} cfu/mL of *E. coli* K-12 cells were inactivated by the solar/ $\text{Cu}_{2-x}\text{S}@PPy$ process in synthetic and real surface water, respectively, while only 0.61 \log_{10} cfu/mL of cells were removed by SODIS alone (Fig. 2g). Surprisingly, the C-D/(C-D + C-H) ratio also decreased from 20.91% to 0.97% (Fig. S17). It suggested that VBNC bacteria were also completely removed in the purified water. Additionally, the reused $\text{Cu}_{2-x}\text{S}@PPy$ maintained a stable disinfection performance of 99.99% for *E. coli* K-12 within 3 cycles (Fig. S18).

The leakage contents of Cu ions were only 0.069 and 0.048 mg/L in water samples after the solar/Cu_{2-x}S and solar/Cu_{2-x}S@PPy treatment, respectively (Table S3), suggesting that the carbon coating of PPy prevents the leakage of metal ions [58]. The total residual Cu content and decomposition of PPy in the purified water were only 0.090 mg/L and 2.14 mg/L as C (Table S3), respectively, which was lower than the limiting value in the Standards for drinking water quality (GB5749–2022, China). Moreover, a series of tests were further performed to evaluate the nontoxicity of the purified water. The photobacterium *Vibrio fischeri* bioassay suggested that Cu_{2-x}S@PPy and the purified water have no acute toxicity since the inhibition rate of luminous was lower than 10% (Figs. S19–S20) [58]. From Fig. S21, the *umu*-chromo test according to International Standard ISO 13829 demonstrated that the genotoxicity of the purified water sample was quite low because the UMU induction ratio was lower than 1.5 (the threshold of genotoxicity) [59–61]. Thus, the secondary pollution was negligible in the solar/Cu_{2-x}S@PPy disinfection system. Taken together, the above results suggest that the solar/Cu_{2-x}S@PPy process has great potential in real-world applications for decentralized, household, or emergency disinfection purposes in rural, isolated, or wild areas.

3.3. Disinfection mechanisms

3.3.1. Self-supply-activation of H₂O₂ and ROSs determination

One of the key motivations of this study is that the combination of Cu_{2-x}S and PPy can boost the in-situ activation of self-supply H₂O₂ for ROSs production and enhanced disinfection. The H₂O₂ production was first monitored. As shown in Fig. 3a, a negligible amount of H₂O₂ was accumulated in the solar/Cu_{2-x}S process, while the concentration of H₂O₂ in the solar/PPy process reached 240.74 μmol/g under identical experimental conditions (Fig. 3a). However, the H₂O₂ production was sharply reduced to 43.98 μmol/g in the N₂ atmosphere (Fig. S23). These results demonstrated that PPy was good at reducing oxygen to form H₂O₂. Interestingly, the H₂O₂ production in the solar/Cu_{2-x}S@PPy process dropped to 46.30 μmol/g. Although a higher concentration of H₂O₂ was generated in the solar/PPy process than in the solar/Cu_{2-x}S@PPy process, the inactivation rate was lower in the solar/PPy process (as discussed in Section 3.2), indicating that H₂O₂ was not the

dominant species that led to the inactivation. It is hypothesized that H₂O₂ was in situ activated by Cu_{2-x}S@PPy, which generated ROSs for enhanced disinfection [62].

To demonstrate that H₂O₂ was in-situ activated and other ROSs were produced, quenching tests and electron spin resonance (ESR) analysis were carried out (the details of principles of each quencher are shown in Text S16). From Fig. 3b, the inactivation was inhibited to different extents in the presence of horseradish peroxidase (HRP, H₂O₂ scavenger), TEMPOL (•O₂ scavenger), furfuryl alcohol (FFA, ¹O₂ scavenger), and isopropanol (IPA, •OH scavenger), with the inactivation rate decreasing from 6.57 to 2.47, 3.05, 3.41, and 5.24 log₁₀ cfu/mL respectively. It was noted that the addition of quenchers had a negligible effect on bacterial activity (Fig. S24). The quenching test results suggested that •O₂ and ¹O₂, rather than •OH, were the predominant ROSs responsible for enhanced disinfection. The highest inhibitory effect of HRP was because H₂O₂ is the precursor of these ROSs (e.g., •O₂ and ¹O₂) [17].

ESR analysis further detected the transformation processes of ROSs. As shown in Fig. 3c, distinct 4-fold peaks of DMPO-•O₂ were identified after 2-min irradiation, after which their intensity kept dropping with prolonged irradiation time. It implied that •O₂ acted as an intermediary for the generation of other ROSs. In contrast, the characteristic peaks of TEMP-¹O₂ were observed within 2 min, but their intensity showed an increasing trend (Fig. 3d). Moreover, the intensity of TEMP-¹O₂ dramatically dropped after the addition of TEMPOL (Fig. S25), suggesting that the oxidation of •O₂ was the major source of ¹O₂ [63,64]. With the prolonged irradiation time, the peaks of DMPO-•OH were barely observed (Fig. 3e). Additionally, the addition of IPA had a negligible effect on the signal of the DMPO-•O₂ peak and TEMP-¹O₂ peak (Fig. S26). The results suggested that the contribution of •OH to the solar/Cu_{2-x}S@PPy system was extremely weak. The ESR results were consistent with the quenching test results and further supported that •O₂ and ¹O₂, rather than •OH, were the predominant ROSs responsible for enhanced disinfection. Based on the time-dependent revolution of ROSs and a series of quenching tests, it was anticipated that H₂O₂ was firstly activated to •O₂ on the Cu–N bridge, followed by the oxidation of •O₂ to ¹O₂.

To verify the stability of the active site (i.e., the electron-poor Cu sites), the recycled Cu_{2-x}S@PPy was detected by the XPS analysis. Interestingly, after the activation of H₂O₂, the valence state of Cu

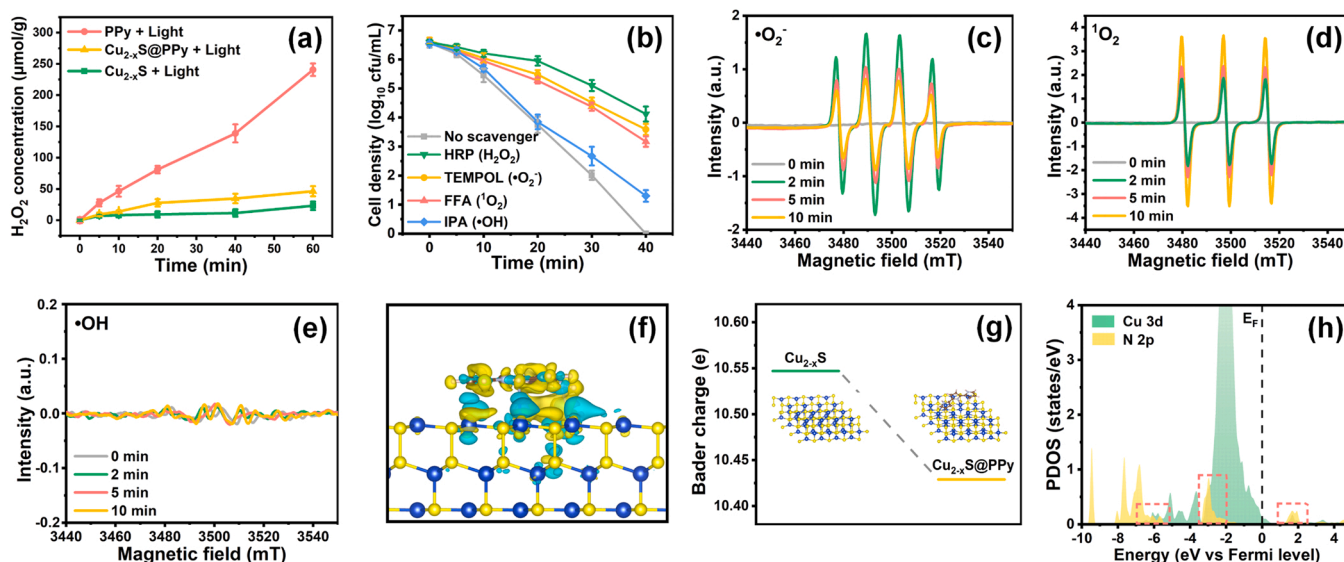


Fig. 3. (a) H₂O₂ photo-production curves of Cu_{2-x}S, PPy, and Cu_{2-x}S@PPy; (b) ROSs quenching tests in the solar/Cu_{2-x}S@PPy system (experimental conditions: [HRP] = [FFA] = [IPA] = [TEMPOL] = 1.0 mM, [Cu_{2-x}S@PPy] = 0.2 mg/mL, optical power density ≈ 2000 W/m², pH = 7); ESR spectra of •O₂ (c), ¹O₂ (d), and •OH (e) generated in the solar/Cu_{2-x}S@PPy system with prolonged time; (f) Charge density difference iso-surface of the Cu_{2-x}S@PPy model (blue and yellow represent electron-deficient and electron accumulation regions, respectively); (g) Bader charge diagrams of the Cu atoms in Cu_{2-x}S and Cu_{2-x}S@PPy; (h) PDOS of the surface atoms in Cu_{2-x}S@PPy with E_F set as zero.

remained stable (Table S4). Thus, the process of ROSs transformation can be summarized as an “electron pump” behavior (Scheme 1). After the self-supply of H_2O_2 , H_2O_2 serving as the electron donor was first oxidized to $\bullet\text{O}_2$ on Cu sites, followed by the oxidation of $\bullet\text{O}_2$ to $^1\text{O}_2$ on electron-poor Cu sites as well. The electron-rich N centers with a higher electronegativity in Cu–N bridges extracted electrons from Cu ($\text{H}_2\text{O}_2 \rightarrow \text{Cu} \rightarrow \text{N}$), ensuring the electron donation-acquisition balance on the active sites. The maintenance of the stability of the active sites allows the H_2O_2 activation to proceed efficiently and stably, with the production of more abundant ROSs. Instead of being stored in PPy, the electrons can be transmitted from the N centers to the pyrrole ring and further the polymer chains [65]. Some excessive electrons that move through the polymer chains can fill in the electron-deficient sites in PPy, where electrons were consumed by O_2 . Additionally, photoluminescence (PL) analysis (Fig. S28) suggested that $\text{Cu}_{2-x}\text{S}@PPy$ had a lower electron-hole recombination rate because of the combination of PPy. It implied that rapid electronic transport channels were formed [66,67].

3.3.2. Theoretical insights of Cu–N electron pump

The DFT calculations were conducted to further support the interfacial electron transfer and the origins of the Cu–N electron pump during the H_2O_2 activation on the dual reaction centers. First, the electron distribution in $\text{Cu}_{2-x}\text{S}@PPy$ was visualized via the charge density difference analysis. As shown in Fig. 3 f, electron transfer occurred on the interface between Cu_{2-x}S and PPy, and electrons on Cu sites were pumped by electron-rich N sites [68]. Moreover, the Bader charge values of the specific Cu atom that linked with PPy were calculated to be 10.547 and 10.429 e in Cu_{2-x}S and $\text{Cu}_{2-x}\text{S}@PPy$ structures, respectively (Fig. 3 g), suggesting that electrons transferred from Cu sites to PPy [69]. Additionally, the Fermi level (E_F) of the Cu_{2-x}S surface was more positive than that of PPy (Fig. S30). Thus, the electrons tended to migrate from the S 2p and Cu 3d orbitals in Cu_{2-x}S to PPy to reach the Fermi equilibrium [70]. The theoretical electron transfer pathway was consistent with XPS, FTIR, and EPR results (Fig. 1f–i) and further confirmed the role of the dual reaction centers to maintain electron donation-acquisition balance.

On this basis, we further explored the interfacial interaction of $\text{Cu}_{2-x}\text{S}@PPy$ with special emphasis on electronic orbitals via the partial density of states (PDOS). As for atoms at the surface, Cu 3d states showed significant orbital overlaps with N 2p states in $\text{Cu}_{2-x}\text{S}@PPy$ (Fig. 3 h) compared to Cu 3d and N 2p states in the individual Cu_{2-x}S and PPy (Fig. S31). It implied that electrons can easily transfer from Cu to N atoms via interfacial Cu–N bridges [69,71]. Additionally, from Fig. S32, the CB edge was mainly composed of S 2p, N 2p, and C 2p orbitals, while Cu 3d orbitals occupied the VB of $\text{Cu}_{2-x}\text{S}@PPy$. The metallic d-orbital structures that had more occupied states in VB indicated more active sites [72]. These results further confirmed Cu–N bridges ensure the electron donation-acquisition balance on the active

sites.

3.4. Electron transport action induced cells' inactivation

3.4.1. Electron transport action over Cu–N bridges

Actually, $\text{Cu}_{2-x}\text{S}@PPy$ can directly extract electrons from cell membranes and accelerate bacteria death via the EET action. First, the ζ -potentials of *E. coli* K-12, Cu_{2-x}S , and $\text{Cu}_{2-x}\text{S}@PPy$ were determined to be -45.3 , -10.7 , and $+16.5$ mV, respectively (Fig. 4a). Generally, positively charged PPy can enhance bacterial adhesion of $\text{Cu}_{2-x}\text{S}@PPy$ via a strong electrostatic attraction, leading to direct attacks from ROSs and heat. It may also destroy cell membranes and disrupt the balance of proton transfer via electron extraction [22,31,56]. Second, the electron extraction process from cells to catalysts was explored via LSV curves. As shown in Fig. 4b, compared to the individual $\text{Cu}_{2-x}\text{S}@PPy$, the $\text{Cu}_{2-x}\text{S}@PPy$ sample with live *E. coli* had a larger saturation current in the dark condition, indicating that live cells can supply electrons for bacterial current [73,74]. On the contrary, the saturation current became smaller than $\text{Cu}_{2-x}\text{S}@PPy$ when dead bacterial cells were introduced. It suggested that cellular metabolic activity was essential in electron transfer. Moreover, a larger saturation current would be generated under irradiation. Additionally, electrochemical impedance spectroscopy (EIS) suggested that $\text{Cu}_{2-x}\text{S}@PPy$ exhibited lower electrochemical impedance and stronger electron transport capability than Cu_{2-x}S (Fig. S33) [75]. It has been reported that interfacial bond bridges which led to the formation of the built-in electron field also gave rise to the steady electron transfer from cells to catalysts [73,74].

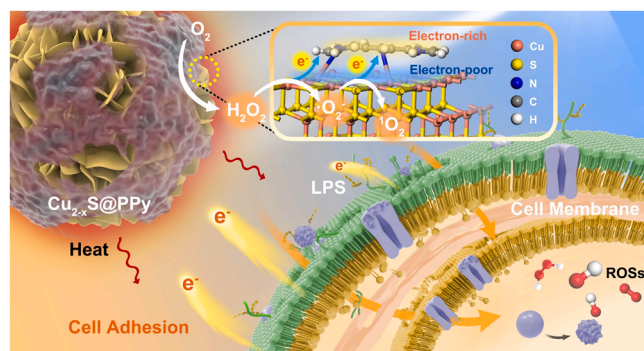
The electron extraction ability was further detected by KPFM measurements. Fig. S34 displays the 3D atomic force microscope (AFM) phase image of the as-prepared bacterial sample, and three *E. coli* cells adhering to the $\text{Cu}_{2-x}\text{S}@PPy$ substrate can be observed. As shown in the corresponding KPFM results (Fig. 4c), the values of the contact potential difference (V_{CPD}) decreased after 10-min treatment without irradiation, suggesting that bacteria were losing free electrons on outer membranes. Moreover, five areas were selected at random to quantitatively detect V_{CPD} and the work function (ϕ_s), and the calculation process was listed in Table S5. The average V_{CPD} of untreated cells was 0.288 V, and the average ϕ_s was calculated to be 4.012 eV. After 10-min contact in the dark, the average value of V_{CPD} dropped to 0.266 V and the average ϕ_s increased to 4.034 eV. It suggested that electrons on outer membranes transfer to $\text{Cu}_{2-x}\text{S}@PPy$ [31].

3.4.2. Interfacial interaction between $\text{Cu}_{2-x}\text{S}@PPy$ and cell membranes

To further detect the interaction action, the interfacial interaction sites between $\text{Cu}_{2-x}\text{S}@PPy$ and bacterial cell membrane were identified via FTIR and XPS analysis. As shown in Fig. 4d, the characteristic peaks at 1079 and 1236 cm^{-1} were attributed to the HPO_4^{2-} and PO_2 absorption band on lipopolysaccharide (LPS), respectively [76,77]. After interaction with $\text{Cu}_{2-x}\text{S}@PPy$, they shifted to 1060 and 1224 cm^{-1} , respectively, whose intensity also met a decline. Additionally, the intensity of the $-\text{COOH}$ stretching band on LSP (1395 cm^{-1}) sharply decreased after interaction with $\text{Cu}_{2-x}\text{S}@PPy$ [76]. LPS is the main component on the outer membrane of *E. coli*. These results indicated that the phosphoryl group and $-\text{COOH}$ on LPS had a strong interaction with the $\text{Cu}_{2-x}\text{S}@PPy$ interface and LPS was seriously destroyed after the solar/ $\text{Cu}_{2-x}\text{S}@PPy$ treatment. Moreover, from the XPS results (Fig. 4e), the binding energy of P 2p exhibited higher energy after being treated with $\text{Cu}_{2-x}\text{S}@PPy$ in the dark, implying that the electrons on the phosphoryl group were pumped by $\text{Cu}_{2-x}\text{S}@PPy$ [76]. Therefore, it can be speculated that the anionic phosphate and carboxyl groups on LPS offer potential interaction sites for electron extraction with positive-charged $\text{Cu}_{2-x}\text{S}@PPy$ [76, 78].

3.4.3. Molecular-level changes of bacteria cells due to electron extraction

The change in electron acceptors from cellular components (e.g., quinone) to $\text{Cu}_{2-x}\text{S}@PPy$ may result in membrane depolarization, lipid



Scheme 1. Proposed mechanisms of microorganisms' inactivation in the solar/ $\text{Cu}_{2-x}\text{S}@PPy$ system.

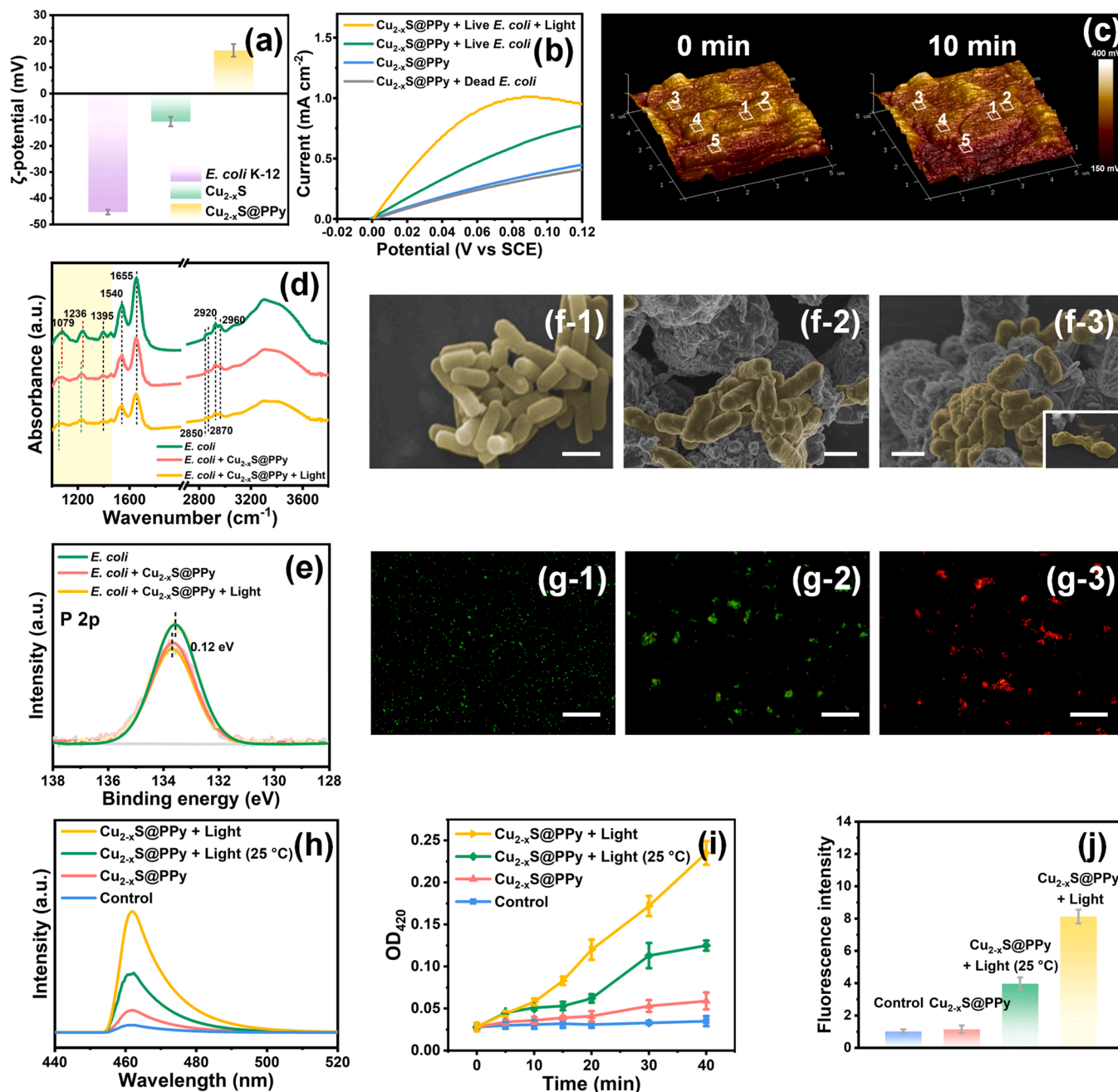


Fig. 4. (a) ζ -potentials of *E. coli* K-12, Cu_{2-x}S , and $\text{Cu}_{2-x}\text{S}@PPy$; (b) LSV curves of $\text{Cu}_{2-x}\text{S}@PPy$ with *E. coli* K-12 under different conditions; (c) 3D KPFM measurement of *E. coli* K-12 adhered on $\text{Cu}_{2-x}\text{S}@PPy$; FTIR analysis (d) and high-resolution XPS spectra of P 2p (e) of $\text{Cu}_{2-x}\text{S}@PPy$ and *E. coli*; SEM images of *E. coli* K-12 before (f-1) and after being exposed to $\text{Cu}_{2-x}\text{S}@PPy$ with 0-min (f-2) and 40-min irradiation time (f-3) (scale bar = 2 μm), and the corresponding fluorescence microscopic images (g) (scale bar = 100 μm); Cellular outer (h) and inner membrane permeability (i) of *E. coli* K-12 in different systems; (j) Fluorescent intensity of intracellular ROS.

extraction, and changes in the physiological state, which accelerated cellular inactivation [73]. On this basis, we explored the changes of bacteria cells at the molecular level during the solar/ $\text{Cu}_{2-x}\text{S}@PPy$ disinfection process by placing emphasis on how EET action accelerated attack from ROSs and heat. We first identify the membrane potential on cytoplasmic membranes induced by the loss of membrane electrons. From Fig. S35 and Text S17, $\text{Cu}_{2-x}\text{S}@PPy$ induced the loss of membrane potential of *E. coli* K-12, which was further reduced under irradiation. Notably, the depolarization of electrical potential across cytoplasmic membranes inhibited ATP generation during the respiratory process. As displayed in Fig. S36, ATP contents of *E. coli* cells dramatically decreased from 11.7 to 0.5×10^{-9} mmol/cell after 40-min treatment, suggesting

that cells lost their metabolic activity. The cutoff of the cellular respiratory chain would result in reduced levels of antioxidant enzymes toward ROSs and heat shock proteins towards heat, accelerating bacterial inactivation [56,79].

As for cellular structure and morphologies during inactivation, *E. coli* cells displayed an intact structure and smooth surface before treatment (Fig. 4f-1). After being exposed to $\text{Cu}_{2-x}\text{S}@PPy$ in the dark, cells were closely attached to $\text{Cu}_{2-x}\text{S}@PPy$ owing to the strong electrostatic attraction and topological interactions (Fig. 4f-2). Additionally, EET deformed cell envelopes with some bulges and pits on the membranes in the dark because of the destructive extraction of lipid molecules in conjunction with electron loss [80]. Moreover, cell membranes further

shrank and deformed after 40-min irradiation, and even thermal ablation can be observed (Fig. 4f–3). The results were coincident with the fluorescent staining tests (Fig. 4 g). Simultaneously, the flow cytometric analysis showed that the damage rate of cell membranes increased from 0.69% to 95.25% (Fig. S37) after treatment. The contents of malondialdehyde (MDA) were monitored, which is one of the typical lipid peroxidation products in the oxidation of *E. coli* cell membranes [81]. From Fig. S38, the MDA content increased from 0.21 to 0.62 nmol/mL after 40-min solar/Cu_{2-x}S@PPy treatment, indicating that the lipid on cell membranes was oxidized by ROSs. FTIR spectra (Fig. 4d) confirmed the decomposition of cellular components. Characteristic peaks of amide on LPS and proteins appeared at 1540 and 1655 cm⁻¹ [76,82]. The peaks at 2870 and 2960 cm⁻¹ were related to the $\nu_a(\text{CH}_3)$ mainly on lipids while $\nu_a(\text{CH}_2)$ appeared at 2850 and 2920 cm⁻¹ [82]. Their intensity dramatically decreased after the solar/Cu_{2-x}S@PPy reaction owing to the oxidation and degradation of lipids and proteins.

Moreover, the ANS fluorescence probe and ONPG probe were used to quantitatively detect the outer and inner membrane permeability of bacteria, respectively (Fig. 4h–i). Compared to the control sample, the higher fluorescence intensity of ANS and higher value of OD₄₂₀ in the Cu_{2-x}S@PPy sample in the dark indicated that EET enhanced outer and inner cell membrane permeability. By conducting the reaction at the 25 °C-water bath to eliminate heat (the green line), we found that ROSs' attack greatly affected cell membrane permeability. Meanwhile, the solar/Cu_{2-x}S@PPy system had the highest value after 40-min irradiation, indicating that heat also accelerated membrane destruction. These results suggested that the direct electron extraction of Cu_{2-x}S@PPy can rapidly destroy the structure of cell membranes that serve as barriers to outside attacks, which made cells more vulnerable to ROSs and heat generated in the solar/Cu_{2-x}S@PPy system. Additionally, EET, ROSs, and heat worked synergistically on the deformation and dysfunction of cell membranes.

The intracellular ROSs levels were detected by using DCF as the fluorescence probe. Without light, the fluorescent intensity did not increase significantly compared to the control group (Fig. 4j) because limited ROSs can be reduced by the intracellular enzyme-like components (e.g., GSH) [73]. However, the enhanced fluorescent intensity under irradiation in a 25 °C water bath implied that ROSs can stimulate oxidative stress in bacterial cells. The fluorescent intensity became stronger without cooling, suggesting that the thermal effect further accelerated the intracellular ROSs accumulation and stimulate oxidative stress. Additionally, from Fig. S39, the decrease of GSH contents with prolonged irradiation time with Cu_{2-x}S@PPy indicated that the intracellular antioxidation system was severely destroyed, resulting in ROSs accumulation and endogenous damage. In short, the EET action induced by the Cu_{2-x}S@PPy electron pump accelerated the membrane depolarization, destruction of cell membranes, and loss of metabolic activity. Thus, cells became more vulnerable to ROSs and heat. These actions synergistically worked on destroying cell membranes, breaking cellular respiratory chains, inducing a burst of intracellular ROSs, and depriving cellular self-defence/repair ability, ultimately resulting in bacterial inactivation, even at a VBNC state (Scheme 1).

4. Conclusions

Cost-effective and low-carbon disinfection technologies are urgently needed to tackle the challenges of water-borne microorganisms, especially in undeveloped, wild, or disaster-stricken areas. We developed and introduced a photo-Fenton-like system over Cu_{2-x}S@PPy with high disinfection efficiency in natural water matrixes and multiple types of reactors. The key mechanisms responsible for promising disinfection performance include that (i) the formation of Cu–N bridge-based “electron pump” in the catalyst worked efficiently in the activation of self-supplied H₂O₂; (ii) Cu_{2-x}S@PPy strongly interacted with cell membranes on LPS and the electron extraction from cell membranes to the catalyst promoted the damage of cell membranes. Two key points

that disclose the knowledge advancement in the field of enhanced SODIS are highlighted in this work: (i) the overlooked role of nonradical pathways (i.e., ¹O₂ attack and the EET action) has been highlighted; and (ii) the EET pathway contributes significantly to cell membrane damage and makes cells more vulnerable to ROSs and heat. The findings provide a novel and affordable solution (e.g., by using the natural sulfur minerals for facile synthesis of catalysts) for rapid and complete inactivation of pathogens in potable water, which can assist rural and underdeveloped areas in achieving SDG 6.1.

CRediT authorship contribution statement

Zhuoyun Tang: Methodology, Validation, Formal analysis, Investigation, Data curation, Writing – original draft, Visualization. **Wei Qu:** Methodology, Validation, Investigation, Data curation, Software. **Zhuohang Lin:** Formal analysis, Investigation, Data curation. **Junjie Li:** Validation, Data curation. **Peizhi Wu:** Investigation, Visualization. **Qiyu Lian:** Software, Supervision. **Chun He:** Writing – review & editing. **Ran Yin:** Conceptualization, Supervision, Writing – review & editing. **Po Keung Wong:** Conceptualization, Supervision. **Dehua Xia:** Conceptualization, Supervision, Funding acquisition, Writing – review & editing.

Declaration of Competing Interest

The authors declare that they have no known competing financial interests or personal relationships that could have appeared to influence the work reported in this paper.

Data Availability

Data will be made available on request.

Acknowledgments

The authors thank the National Natural Science Foundation of China (No. 21876212, 21976214, 41603097, 21673086, 52070195, 42207056), Guangdong Basic and Applied Basic Research Foundation (2022B1515020097, 2019A1515011015, 2021A1515110224), Opening Fund of the State Key Laboratory of Environmental Geochemistry (SKLEG2022221), the Science and Technology Program of Guangzhou (201904010353) and Fundamental Research Funds for the Central Universities, Sun Yat-sen University (13lgjc10, 19lgpy157, 22lgqb21) for financially supporting this work.

Appendix A. Supporting information

Supplementary data associated with this article can be found in the online version at doi:10.1016/j.apcatb.2023.123047.

References

- [1] C. Frick, J. Vierheilig, T. Nadiotis-Tsaka, S. Ixenmaier, R. Linke, G.H. Reischer, J. Komma, A.K.T. Kirschner, R.L. Mach, D. Savio, D. Seidl, A.P. Blaschke, R. Sommer, J. Drex, A.H. Farnleitner, Elucidating fecal pollution patterns in alluvial water resources by linking standard fecal indicator bacteria to river connectivity and genetic microbial source tracking, *Water Res.* 184 (2020), 116132.
- [2] G. Wen, Z. Liang, X. Xu, R. Cao, Q. Wan, G. Ji, W. Lin, J. Wang, J. Yang, T. Huang, Inactivation of fungal spores in water using ozone: Kinetics, influencing factors and mechanisms, *Water Res.* 185 (2020), 116218.
- [3] P.J.J. Alvarez, C.K. Chan, M. Elimelech, N.J. Halas, D. Villagrán, Emerging opportunities for nanotechnology to enhance water security, *Nat. Nanotechnol.* 13 (2018) 634–641.
- [4] L. Zhu, X. Shuai, L. Xu, Y. Sun, Z. Lin, Z. Zhou, L. Meng, H. Chen, Mechanisms underlying the effect of chlorination and UV disinfection on VBNC state *Escherichia coli* isolated from hospital wastewater, *J. Hazard. Mater.* 423 (2022), 127228.
- [5] T. Jäger, J. Alexander, S. Kirchen, A. Dötsch, A. Wieland, C. Hiller, T. Schwartz, Live-dead discrimination analysis, qPCR assessment for opportunistic pathogens, and population analysis at ozone wastewater treatment plants, *Environ. Pollut.* 232 (2018) 571–579.

- [6] J.J. Alvear-Daza, A. García-Barco, P. Osorio-Vargas, H.M. Gutierrez-Zapata, J. Sanabria, J.A. Rengifo-Herrera, Resistance and induction of viable but non culturable states (VBNC) during inactivation of *E. coli* and *Klebsiella pneumoniae* by addition of H₂O₂ to natural well water under simulated solar irradiation, *Water Res.* 188 (2021), 116499.
- [7] Y. Xia, Q. Wan, X. Xu, R. Cao, Y. Li, J. Wang, H. Xu, T. Huang, G. Wen, Solar disinfection of fungal spores in water: Kinetics, influencing factors, mechanisms and regrowth, *Chem. Eng. J.* 428 (2022), 132065.
- [8] J. Ndounla, D. Spuhler, S. Kenfack, J. Wéthé, C. Pulgarin, Inactivation by solar photo-fenton in pet bottles of wild enteric bacteria of natural well water: Absence of re-growth after one week of subsequent storage, *Appl. Catal. B: Environ.* 129 (2013) 309–317.
- [9] L. Lyu, G. Yu, L. Zhang, C. Hu, Y. Sun, 4-Phenoxyphenol-functionalized reduced graphene oxide nanosheets: a metal-free Fenton-like catalyst for pollutant destruction, *Environ. Sci. Technol.* 52 (2018) 747–756.
- [10] S. Zhan, H. Zhang, X. Mi, Y. Zhao, C. Hu, L. Lyu, Efficient Fenton-like process for pollutant removal in electron-rich/poor reaction sites induced by surface oxygen vacancy over cobalt-zinc oxides, *Environ. Sci. Technol.* 54 (2020) 8333–8343.
- [11] W. Qu, C. Chen, Z. Tang, D. Xia, D. Ma, Y. Huang, Q. Lian, C. He, D. Shu, B. Han, Electron-rich/poor reaction sites enable ultrafast confining Fenton-like processes in facet-engineered BiOI membranes for water purification, *Appl. Catal. B: Environ.* 304 (2022), 120970.
- [12] W. Qu, Z. Tang, W. Liu, Y. Liao, Y. Huang, D. Xia, Q. Lian, S. Tian, C. He, D. Shu, Self-accelerating interfacial catalytic elimination of gaseous sulfur-containing volatile organic compounds as microbubbles in a facet-engineered three-dimensional BiOCl sponge Fenton-like process, *Environ. Sci. Technol.* 56 (2022) 11657–11669.
- [13] N. Zhu, S. Wang, C. Tang, P. Duan, L. Yao, J. Tang, P.K. Wong, T. An, D. Dionysiou, Y. Wu, Protection mechanisms of periphytic biofilm to photocatalytic nanoparticle exposure, *Environ. Sci. Technol.* 53 (2019) 1585–1594.
- [14] D. Awfa, M. Ateia, M. Fujii, C. Yoshimura, Photocatalytic degradation of organic micropollutants: Inhibition mechanisms by different fractions of natural organic matter, *Water Res.* 174 (2020), 115643.
- [15] L. Ge, Y. Yue, W. Wang, F. Tan, S. Zhang, X. Wang, X. Qiao, P.K. Wong, Efficient degradation of tetracycline in wide pH range using MgNCN/MgO nanocomposites as novel H₂O₂ activator, *Water Res.* 198 (2021), 117149.
- [16] W. Ren, C. Cheng, P. Shao, X. Luo, H. Zhang, S. Wang, X. Duan, Origins of electron-transfer regime in persulfate-based nonradical oxidation processes, *Environ. Sci. Technol.* 56 (2022) 78–97.
- [17] T. Li, L. Ge, X. Peng, W. Wang, W. Zhang, Enhanced degradation of sulfamethoxazole by a novel Fenton-like system with significantly reduced consumption of H₂O₂ activated by g-C₃N₄/MgO composite, *Water Res.* 190 (2021), 116777.
- [18] W. Wang, H. Xie, G. Li, J. Li, P.K. Wong, T. An, Visible light-induced marine bacterial inactivation in seawater by an in situ photo-Fenton system without additional oxidants: Implications for ballast water sterilization, *ACS EST Water* 1 (2021) 1483–1494.
- [19] Y. Chu, X. Zheng, J. Fan, Preparation of sodium and boron co-doped graphitic carbon nitride for the enhanced production of H₂O₂ via two-electron oxygen reduction and the degradation of 2,4-DCP via photocatalytic oxidation coupled with Fenton oxidation, *Chem. Eng. J.* 431 (2022), 134020.
- [20] L. Zhang, S.-S. Wan, C.-X. Li, L. Xu, H. Cheng, X.-Z. Zhang, An adenosine triphosphate-responsive autocatalytic Fenton nanoparticle for tumor ablation with self-supplied H₂O₂ and acceleration of Fe(III)/Fe(II) conversion, *Nano Lett.* 18 (2018) 7609–7618.
- [21] H. Luo, J. Qi, M. Zhou, G. Liu, Y. Lu, R. Zhang, C. Zeng, Enhanced electron transfer on microbial electrosynthesis biocathode by polypyrrole-coated acetogens, *Bioresour. Technol.* 309 (2020), 123322.
- [22] E.N. Zare, T. Agarwal, A. Zarepour, F. Pinelli, A. Zarrabi, F. Rossi, M. Ashrafzadeh, A. Maleki, M.-A. Shabbazi, T.K. Maiti, R.S. Varma, F.R. Tay, M.R. Hamblin, V. Mattoli, P. Makvandi, Electroconductive multi-functional polypyrrole composites for biomedical applications, *Appl. Mater. Today* 24 (2021), 101117.
- [23] X. Gao, M. Wei, D. Ma, X. Yang, Y. Zhang, X. Zhou, L. Li, Y. Deng, W. Yang, Engineering of a hollow-structured Cu_{2-x}S nano-homojunction platform for near infrared-triggered infected wound healing and cancer therapy, *Adv. Funct. Mater.* 31 (2021) 2106700.
- [24] A. Nain, S.C. Wei, Y.F. Lin, Y.T. Tseng, R.P. Mandal, Y.F. Huang, C.C. Huang, F. G. Tseng, H.T. Chang, Copper sulfide nanoassemblies for catalytic and photoresponsive eradication of bacteria from infected wounds, *ACS Appl. Mater. Interface* 13 (2021) 7865–7878.
- [25] H. Peng, G. Ma, K. Sun, J. Mu, H. Wang, Z. Lei, High-performance supercapacitor based on multi-structural CuS/polypyrrole composites prepared by in situ oxidative polymerization, *J. Mater. Chem. A* 2 (2014) 3303.
- [26] W. Chen, Z. Wang, M. Tian, G. Hong, Y. Wu, M. Sui, M. Chen, J. An, F. Song, X. Peng, Integration of TADF photosensitizer as “electron pump” and BSA as “electron reservoir” for boosting Type I photodynamic therapy, *J. Am. Chem. Soc.* 145 (2023) 8130–8140.
- [27] P. Liu, Z. Huang, S. Yang, J. Du, Y. Zhang, R. Cao, C. Chen, L. Li, T. Chen, G. Wang, D. Rao, X. Zheng, X. Hong, Support amorphization engineering regulates single-atom Ru as an electron pump for nitrogen photofixation, *ACS Catal.* 12 (2022) 8139–8146.
- [28] P. Zhou, G. Hai, G. Zhao, R. Li, X. Huang, Y. Lu, G. Wang, CeO₂ as an “electron pump” to boost the performance of Co₄N in electrocatalytic hydrogen evolution, oxygen evolution and biomass oxidation valorization, *Appl. Catal. B: Environ.* 325 (2023), 122364.
- [29] M. Inyang, E. Dickenson, The potential role of biochar in the removal of organic and microbial contaminants from potable and reuse water: a review, *Chemosphere* 134 (2015) 232–240.
- [30] T. Do Minh, J. Song, A. Deb, L. Cha, V. Srivastava, M. Sillanpää, Biochar based catalysts for the abatement of emerging pollutants: a review, *Chem. Eng. J.* 394 (2020), 124856.
- [31] N.M. Das, A.K. Singh, D. Ghosh, D. Bandyopadhyay, Graphene oxide nanohybrids for electron transfer-mediated antimicrobial activity, *Nanoscale Adv.* 1 (2019) 3727–3740.
- [32] Q.W. Tian, M.H. Tang, Y.G. Sun, R.J. Zou, Z.G. Chen, M.F. Zhu, S.P. Yang, J. L. Wang, J.H. Wang, J.Q. Hu, Hydrophilic flower-like CuS superstructures as an efficient 980 nm laser-driven photothermal agent for ablation of cancer cells, *Adv. Mater.* 23 (2011) 3542–3547.
- [33] F. Cao, L. Zhang, H. Wang, Y. You, Y. Wang, N. Gao, J. Ren, X. Qu, Defect-rich adhesive nanozymes as efficient antibiotics for enhanced bacterial inhibition, *Angew. Chem. Intern. Ed.* 58 (2019) 16236–16242.
- [34] L. Wang, F. Gao, A. Wang, X. Chen, H. Li, X. Zhang, H. Zheng, R. Ji, B. Li, X. Yu, J. Liu, Z. Gu, F. Chen, C. Chen, Defect-rich adhesive molybdenum disulfide/rGO vertical heterostructures with enhanced nanzyme activity for smart bacterial killing application, *Adv. Mater.* 32 (2020), e2005423.
- [35] S. Zuo, Z. Guan, F. Yang, D. Xia, D. Li, Reactive oxygen species regulation and synergistic effect for effective water purification through Fenton-like catalysis on single-atom Cu–N sites, *J. Mater. Chem. A* 10 (2022) 10503–10513.
- [36] Y. Li, S. Yan, X. Jia, J. Wu, J. Yang, C. Zhao, S. Wang, H. Song, X. Yang, Uncovering the origin of full-spectrum visible-light-responsive polypyrrole supramolecular photocatalysts, *Appl. Catal. B: Environ.* 287 (2021), 119926.
- [37] Z. Yin, W. Fan, Y. Ding, J. Li, L. Guan, Q. Zheng, Shell structure control of PPy-modified CuO composite nanoleaves for lithium batteries with improved cyclic performance, *ACS Sustain. Chem. Eng.* 3 (2015) 507–517.
- [38] Y. Wang, L. Cao, J. Li, L. Kou, J. Huang, Y. Feng, S. Chen, Cu/Cu₂O@PPy nanowires as a long-life and high-capacity anode for lithium ion battery, *Chem. Eng. J.* 391 (2020), 123597.
- [39] Z. Fang, Y. Liu, J. Qi, Z.-F. Xu, T. Qi, L. Wang, Establishing a high-speed electron transfer channel via CuS/MIL-Fe heterojunction catalyst for photo-Fenton degradation of acetaminophen, *Appl. Catal. B: Environ.* 320 (2023), 121979.
- [40] Z. Cui, S. Song, H. Liu, Y. Zhang, F. Gao, T. Ding, Y. Tian, X. Fan, X. Li, Synergistic effect of Cu⁺ single atoms and Cu nanoparticles supported on alumina boosting water-gas shift reaction, *Appl. Catal. B: Environ.* 313 (2022), 121468.
- [41] A.M. Abdel-Mageed, B. Rungtaweeworant, M. Parlinska-Wojtan, X. Pei, O. M. Yaghi, R.J. Behm, Highly active and stable single-atom Cu catalysts supported by a metal-organic framework, *J. Am. Chem. Soc.* 141 (2019) 5201–5210.
- [42] F. Scholten, I. Sinev, M. Bernal, B. Roldan Cuenya, Plasma-modified dendritic Cu catalyst for CO₂ electroreduction, *ACS Catal.* 9 (2019) 5496–5502.
- [43] Y. Li, J. Li, Y. Pan, Z. Xiong, G. Yao, R. Xie, B. Lai, Peroxymonosulfate activation on FeCo₂S₄ modified g-C₃N₄ (FeCo₂S₄-CN): Mechanism of singlet oxygen evolution for nonradical efficient degradation of sulfamethoxazole, *Chem. Eng. J.* 384 (2020), 123361.
- [44] Y. He, H. Rao, K. Song, J. Li, Y. Yu, Y. Lou, C. Li, Y. Han, Z. Shi, S. Feng, 3D hierarchical ZnIn₂S₄ nanosheets with rich Zn vacancies boosting photocatalytic CO₂ reduction, *Adv. Funct. Mater.* 29 (2019) 1905153.
- [45] W. Wu, L. Zhan, W. Fan, J. Song, X. Li, Z. Li, R. Wang, J. Zhang, J. Zheng, M. Wu, H. Zeng, Cu–N dopants boost electron transfer and photooxidation reactions of carbon dots, *Angew. Chem. Int. Ed. Engl.* 54 (2015) 6540–6544.
- [46] R.-R. Cheng, Z.-L. Wu, Y.-L. Hou, J. Dong, J.-Z. Cui, B. Zhao, Three Cu(II) coordination polymers with novel bi-triazole ligand: Synthesis, structure and EPR properties, *Inorg. Chem. Commun.* 51 (2015) 95–98.
- [47] Z. Xie, J. Zhou, J. Wang, C.P. François-Xavier, T. Wintgens, Novel Fenton-like catalyst γ-Cu-Al₂O₃-Bi₁₂O₁₅Cu₆ with electron-poor Cu centre and electron-rich Bi centre for enhancement of phenolic compounds degradation and H₂O₂ utilization: the synergistic effects of σ-Cu-ligand, dual-reaction centres and oxygen vacancies, *Appl. Catal. B: Environ.* 253 (2019) 28–40.
- [48] Z. Hou, J. Chu, C. Liu, J. Wang, A. Li, T. Lin, C.P. François-Xavier, High efficient photocatalytic reduction of nitrate to N₂ by core-shell Ag/SiO₂@cTiO₂ with synergistic effect of light scattering and surface plasmon resonance, *Chem. Eng. J.* 415 (2021), 128863.
- [49] G. Yu, J. Qian, P. Zhang, B. Zhang, W. Zhang, W. Yan, G. Liu, Collective excitation of plasmon-coupled Au-nanochain boosts photocatalytic hydrogen evolution of semiconductor, *Nat. Commun.* 10 (2019) 4912.
- [50] X. Li, H. Jiang, C. Ma, Z. Zhu, X. Song, H. Wang, P. Huo, X. Li, Local surface plasma resonance effect enhanced Z-scheme ZnO/Au/g-C₃N₄ film photocatalyst for reduction of CO₂ to CO, *Appl. Catal. B: Environ.* 283 (2021), 119638.
- [51] X. Shi, L. Wang, W. Dai, X. Dong, Y. Bai, L. Ye, CO₂ photoreduction catalyzed by Cu-deficient Cu_{1.95}S@CuS: Enhanced performance via boosted directional interfacial charge transfer, *ACS Catal.* 8 (2023) 5264–5271.
- [52] X. Yuan, C. Wang, D. Dragoe, P. Beunier, C. Colbeau-Justin, H. Remita, Highly promoted photocatalytic hydrogen generation by multiple electron transfer pathways, *Appl. Catal. B: Environ.* 281 (2021), 119457.
- [53] L. Wang, Y. Feng, K. Wang, G. Liu, Solar water sterilization enabled by photothermal nanomaterials, *Nano Energy* 87 (2021), 106158.
- [54] S. Chen, X. Li, Y. Wang, J. Zeng, C. Ye, X. Li, L. Guo, S. Zhang, X. Yu, Induction of *Escherichia coli* into a VBNC state through chlorination/chloramination and differences in characteristics of the bacterium between states, *Water Res.* 142 (2018) 279–288.
- [55] L. Wang, C. Ye, L. Guo, C. Chen, X. Kong, Y. Chen, L. Shu, P. Wang, X. Yu, J. Fang, Assessment of the UV/chlorine process in the disinfection of *Pseudomonas*

- aeruginosa*: efficiency and mechanism, *Environ. Sci. Technol.* 55 (2021) 9221–9230.
- [56] Z. Tang, R. Yin, W. Qu, H. Liu, H. Luo, D. Xia, Y. Huang, L. Shu, C. He, Flower pollen-based photosensitization process for enhanced solar disinfection of drinking water: Reactor design and inactivation mechanisms, *ACS EST Eng.* 2 (2022) 629–641.
- [57] D. Xia, Q. Chen, Y. Jiao, Q. Lian, M. Sun, C. He, J. Shang, T. Wang, A modified flower pollen-based photothermocatalytic process for enhanced solar water disinfection: photoelectric effect and bactericidal mechanisms, *Water Res.* 217 (2022), 118423.
- [58] R. Zhang, C. Song, M. Kou, P. Yin, X. Jin, L. Wang, Y. Deng, B. Wang, D. Xia, P. K. Wong, L. Ye, Sterilization of *Escherichia coli* by photothermal synergy of WO₃-x/C nanosheet under infrared light irradiation, *Environ. Sci. Technol.* 54 (2020) 3691–3701.
- [59] ISO, Water quality - Determination of the genotoxicity of water and waste water using the *umu*-test (ISO 13829), International Organization for Standardization (2000).
- [60] Y.-Y. Lou, S.-H. Yin, J. Yang, L.-F. Ji, J.-Y. Fang, S.-Q. Zhang, M.-B. Feng, X. Yu, Y.-X. Jiang, S.-G. Sun, MOF-derived single site catalysts with electron-rich Fe–N₄ sites for efficient elimination of trichloroacetamide DBP, *Chem. Eng. J.* 446 (2022), 137060.
- [61] D. Xia, H. Liu, Z. Jiang, T.W. Ng, W.S. Lai, T. An, W. Wang, P.K. Wong, Visible-light-driven photocatalytic inactivation of *Escherichia coli* K-12 over thermal treated natural magnetic sphalerite: Band structure analysis and toxicity evaluation, *Appl. Catal. B: Environ.* 224 (2018) 541–552.
- [62] X. Li, J. He, J. Lu, Y. Zhou, Y. Zhou, In-situ production and activation of H₂O₂ for enhanced degradation of roxarsone by FeS₂ decorated resorcinol-formaldehyde resins, *J. Hazard. Mater.* 424 (2022), 127650.
- [63] X. Yang, X. Ding, S. Wang, J. Mao, L. Cheng, P. Li, H. Chen, Superoxide anion and singlet oxygen dominated faster photocatalytic elimination of nitric oxide over defective bismuth molybdates heterojunctions, *J. Colloid Interface Sci.* 618 (2022) 248–258.
- [64] Y. Nosaka, A.Y. Nosaka, Generation and detection of reactive oxygen species in photocatalysis, *Chem. Rev.* 117 (2017) 11302–11336.
- [65] T.F. Yi, L.Y. Qiu, J. Mei, S.Y. Qi, P. Cui, S. Luo, Y.R. Zhu, Y. Xie, Y.B. He, Porous spherical NiO@NiMoO₄@PPy nanoarchitectures as advanced electrochemical pseudocapacitor materials, *Sci. Bull.* 65 (2020) 546–556.
- [66] J. Zhuang, W. Lai, M. Xu, Q. Zhou, D. Tang, Plasmonic AuNP/g-C₃N₄ nanohybrid-based photoelectrochemical sensing platform for ultrasensitive monitoring of polynucleotide kinase activity accompanying DNase-catalyzed precipitation amplification, *ACS Appl. Mater. Interfaces* 7 (2015) 8330–8338.
- [67] G. Fan, J. Zhan, J. Luo, J. Lin, F. Qu, B. Du, Y. You, Z. Yan, Fabrication of heterostructured Ag/AgCl@g-C₃N₄@UIO-66(NH₂) nanocomposite for efficient photocatalytic inactivation of microcystis *aeruginosa* under visible light, *J. Hazard. Mater.* 404 (2021), 124062.
- [68] D. Ma, W. Liu, Y. Huang, D. Xia, Q. Lian, C. He, Enhanced catalytic ozonation for eliminating CH₃SH via stable and circular electronic metal-support interactions of Si–O–Mn bonds with low Mn loading, *Environ. Sci. Technol.* 56 (2022) 3678–3688.
- [69] F. Li, Z. Lu, T. Li, P. Zhang, C. Hu, Origin of the excellent activity and selectivity of a single-atom copper catalyst with unsaturated Cu–N₂ sites via peroxydisulfate activation: Cu(III) as a dominant oxidizing species, *Environ. Sci. Technol.* 56 (2022) 8765–8775.
- [70] W. Xu, W. Tian, L. Meng, F. Cao, L. Li, Interfacial chemical bond-modulated Z-scheme charge transfer for efficient photoelectrochemical water splitting, *Adv. Energy Mater.* 11 (2021) 2003500.
- [71] J. Zhu, M. Xiao, D. Ren, R. Gao, X. Liu, Z. Zhang, D. Luo, W. Xing, D. Su, A. Yu, Z. Chen, Quasi-covalently coupled Ni–Cu atomic pair for synergistic electroreduction of CO₂, *J. Am. Chem. Soc.* 144 (2022) 9661–9671.
- [72] W. Zhang, C. Fu, J. Low, D. Duan, J. Ma, W. Jiang, Y. Chen, H. Liu, Z. Qi, R. Long, Y. Yao, X. Li, H. Zhang, Z. Liu, J. Yang, Z. Zou, Y. Xiong, High-performance photocatalytic nonoxidative conversion of methane to ethane and hydrogen by heteroatoms-engineered TiO₂, *Nat. Commun.* 13 (2022) 2806.
- [73] G. Wang, K. Tang, Z. Meng, P. Liu, S. Mo, B. Mehrjou, H. Wang, X. Liu, Z. Wu, P. K. Chu, A quantitative bacteria monitoring and killing platform based on electron transfer from bacteria to a semiconductor, *Adv. Mater.* 32 (2020), e2003616.
- [74] G. Wang, H. Feng, A. Gao, Q. Hao, W. Jin, X. Peng, W. Li, G. Wu, P.K. Chu, Extracellular electron transfer from aerobic bacteria to Au-loaded TiO₂ semiconductor without light: a new bacteria-killing mechanism other than localized surface plasmon resonance or microbial fuel cells, *ACS Appl. Mater. Interfaces.* 8 (2016) 24509–24516.
- [75] T. Shi, X. Hou, S. Guo, L. Zhang, C. Wei, T. Peng, X. Hu, Nanohole-boosted electron transport between nanomaterials and bacteria as a concept for nano-bio interactions, *Nat. Commun.* 12 (2021) 493.
- [76] J. Wang, Y. Meng, Z. Jiang, M.T. Sarwar, L. Fu, H. Yang, Engineering nanoclay edges to enhance antimicrobial property against Gram-negative bacteria: understanding the membrane destruction mechanism by contact-kill, *Adv. Funct. Mater.* 33 (2023) 2210406.
- [77] X.-f Li, X.-q Feng, S. Yang, G.-q Fu, T.-p Wang, Z.-x Su, Chitosan kills *Escherichia coli* through damage to be of cell membrane mechanism, *Carbohydr. Polym.* 79 (2010) 493–499.
- [78] J. Liu, L. Sandaklie-Nikolova, X. Wang, J.D. Miller, Surface force measurements at kaolinite edge surfaces using atomic force microscopy, *J. Colloid Interf. Sci.* 420 (2014) 35–40.
- [79] M. Chang, Z. Hou, M. Wang, D. Wen, C. Li, Y. Liu, Y. Zhao, J. Lin, Cu single atom nanozyme based high-efficiency mild photothermal therapy through cellular metabolic regulation, *Angew. Chem. Int. Ed.* 61 (2022), e202209245.
- [80] Y. Tu, M. Lv, P. Xiu, T. Huynh, M. Zhang, M. Castelli, Z. Liu, Q. Huang, C. Fan, H. Fang, R. Zhou, Destructive extraction of phospholipids from *Escherichia coli* membranes by graphene nanosheets, *Nat. Nanotechnol.* 8 (2013) 594–601.
- [81] C. Hu, J. Guo, J. Qu, X. Hu, Photocatalytic degradation of pathogenic bacteria with AgI/TiO₂ under visible light irradiation, *Langmuir* 23 (2007) 4982–4987.
- [82] A. Salman, I. Lapidot, A. Pomerant, L. Tsrar, Z. Hammody, R. Moreh, M. Huleihel, S. Mordechai, Detection of *Fusarium oxysporum* fungal isolates using ATR spectroscopy, *Spectrosc.: Int. J.* 27 (2012) 551–556.